Available online at www.sciencedirect.com

SciVerse ScienceDirect

Ceramics International 39 (2013) 6077–6085

CERAMICS INTERNATIONAL

www.elsevier.com/locate/ceramint

Structural, optical and magnetic properties of $Zn_{1-x}Co_xO$ prepared by the sol–gel route

Gunjan Srinet[a], Prateek Varshney[a], Ravindra Kumar[a,*], Vivek Sajal[a], P.K. Kulriya[b], M. Knobel[c], S.K. Sharma[c]

[a]*Department of Physics & Material Science & Engineering, Jaypee Institute of Information Technology, Noida 201307, Uttar Pradesh, India*
[b]*Inter University Accelerator Centre, Aruna Asaf Ali Marg, New Delhi, India*
[c]*Instituto de Fisica Gleb Wataghin, Universidade Estadual de Campinas (UNICAMP) Campinas, 13.083-859 SP, Brazil*

Received 19 October 2012; received in revised form 9 January 2013; accepted 9 January 2013
Available online 17 January 2013

Abstract

Effects of Co doping on the structural, optical and magnetic properties of ZnO samples prepared by the sol–gel method are reported. The X-ray diffraction, X-ray photoelectron spectroscopy and UV–visible spectroscopy confirmed the substitution of Co ions on Zn sites without changing the wurtzite structure. No segregated secondary phases or Co rich clusters were detected. Optical absorption spectra of the samples exhibit a blue shift in the absorption band edge with increasing dopant concentration. The photoluminescence measurements show a blue shift in UV emission peak with the increase in Co concentration and a slight shift in the green emission band at around 509 nm which gets suppressed for higher sintering temperature. The field dependence of magnetization observed at room temperature exhibits clear ferromagnetic behavior. Efforts have been made to fit the experimental *M–H* data using the magnetic polarons model (BMP) which involves localized carriers and magnetic cations. The calculated concentration of the BMPs is found to be below the typical percolation threshold in ZnO. Thus BMP model alone is not sufficient to explain the room temperature ferromagnetic behavior in ZnO. To know the exact magnetic ordering in the system, we also attempted to fit temperature dependent magnetization curves with the Curie–Weiss Law which shows antiferromagnetic ordering in all samples.

Keywords: D. ZnO; Diluted magnetic semiconductors

1. Introduction

Continuous efforts to develop next generation multifunctional devices are now being extended to the search for new materials which can combine magnetic, electronic and photonic responses. Diluted magnetic semiconductors (DMSs), in which transition metal (TM) ions are introduced into the cationic sites of the host semiconducting lattice, have recently attracted the scientific community because of their potential applications in spintronic and optoelectronic devices [1–3].

The main challenge in the practical utility of these materials is the attainment of room temperature ferromagnetism (RTFM). The prediction of RTFM in some magnetically doped wide band gap semiconductors (II–VI and III–V group semiconductor) has stimulated more attention on the research of these materials [2]. Among II–VI semiconductors, ZnO is a versatile multifunctional candidate with esthetic morphologies, a direct wide band gap (3.3 eV at 300 K), large excitonic binding energy (60 meV), outstanding electro-optic and piezoelectric properties and excellent chemical stability which can be useful in electronics and optoelectronic devices [4,5].

Particularly, TM doped ZnO DMSs have attracted much attention due to theoretical prediction of RTFM followed by experimentally observed RTFM. Dietl et al. [2,6] predicted ZnO and GaN as candidates having a high *Tc* and large magnetization. Later, some contradictory experimental results [7–13] were reported. Co doped ZnO has attracted scientists not only for its RTFM [8], but also

*Corresponding author. Tel.: +91 99 99762428.
E-mail addresses: ravindrakbhatt@gmail.com, ravindra.kumar@jiit.ac.in (R. Kumar).

0272-8842/$ - see front matter © 2013 Elsevier Ltd and Techna Group S.r.l. All rights reserved.
http://dx.doi.org/10.1016/j.ceramint.2013.01.025

its ferromagnetic transport properties. Also, Sato et al. [14] theoretically suggested that RTFM in Co doped ZnO can be stabilized. Ueda et al. [7] reported the RTFM for Co doped ZnO thin films prepared by pulsed laser deposition with a reproducibility of less than 10%. Jin et al. [11] found no signature of ferromagnetism in films grown by laser molecular beam epitaxy. Zhu et al. [12] reported RTFM in two step prepared Co doped ZnO bulks. No bulk ferromagnetism was observed for single phase transition metal doped ZnO, contrary to theoretical results [13].

In spite of extensive studies, understanding the mechanism of magnetism of TM doped ZnO systems still remains a debatable issue, mostly due to the low reproducibility of results from samples prepared by different techniques [15,16]. The RTFM observed for some samples has been attributed to different origins, including the original model of ferromagnetism mediated by free carriers or shallow donor electrons forming bound polarons [17] and alternative explanations such as the formation of secondary magnetic phases [18] and TM rich nanocrystals [19]. Under this scenario, careful experiments are needed to establish the intrinsic and robust magnetism. In the present paper, experimental and theoretical investigations on structural, optical and magnetic properties of Co doped ZnO synthesized by the sol–gel method are reported. The system is found to be ferromagnetic at room temperature and exhibited blue shift in the absorption band edge with increasing Co concentration.

2. Experimental details

Appropriate proportions of high purity zinc acetate [$Zn(CH_3COO)_2\cdot(2H_2O)$] and cobalt acetate [$Co(CH_3COO)_2$] were used to synthesize $Zn_{1-x}Co_xO$ ($x=0.02$, 0.04, and 0.06) using the sol–gel method.

To prepare cobalt doped ZnO samples, 0.1 M zinc acetate solution was prepared in 2-methoxymethanol. Cobalt acetate used as a doping source was added to this solution to attain a Zn:Co ratio of 0.98:0.02, 0.96:0.04 and 0.94:0.06. The resulting solution was mixed overnight at 60 °C using a magnetic stirrer to achieve a homogeneous solution. Sols were stable and homogeneous; no particulates or precipitates were visible. Then, the final solution was dried in an oven at 100 °C for 24 h and then ground. Afterwards, the dried gel was calcined at 400 °C for 2 h. Further, samples were compacted into pellets by pressing in a dye by a hydraulic (6–8*t*) pressure machine. Pellets were 0.5 mm thick and had a 10 mm diameter. The sintering temperature and time are very crucial in deciding the properties of the DMS material. The sintering was done by placing pellets in a ceramic boat at 400 °C and 500 °C.

The X-ray diffraction (XRD) of sintered pellets was carried out by a D-8 Advanced Bruker X-ray diffractometer with CuKα ($\lambda=1.5406$ Å) radiation. The XRD data was analyzed by Full Proof Software (Rietveld Methods). X-ray photoelectron spectra (XPS) of Co doped ZnO pellets have been recorded using a Perkin–Elmer (PH1-1257) series with AlKα X-ray source ($h\nu=1486.6$ eV). The pass energy for survey spectra was 100 eV and 40 eV for core level scan. Absorption spectra were carried out by a Perkin–Elmer Lambda-35 UV–visible spectrometer in the wavelength range of 300–800 nm. Photoluminescence spectra of samples were acquired using xenon flash lamp as excitation source by Perkin–Elmer Lamda luminescence spectrophotometer. Both experiments were done for powder samples sonicated in ethanol medium. A super-conducting Quantum Interference Device [SQUID (Quantum Design, MPMS-XL)] of the powder was used to study the magnetic properties of samples.

3. Results and discussion

3.1. Structural characterization

The X-ray diffraction study is performed to investigate effects of Co doping and sintering temperature on the crystal structure of the ZnO. After the final cycle of Rietveld refinement, XRD patterns of two sets of $Zn_xCo_{1-x}O$ ($x=0.02$, 0.04 and 0.06) samples sintered at 400 °C and 500 °C are shown in Figs. 1 and 2, respectively.

Rietveld refinements on the XRD data were done by selecting the space group *P63 mc*. Observed and calculated values were perfectly matching as can be seen from figures. Values of χ^2 were in the range 1.10–1.23, which are good for estimations, as the profile fitting procedure adopted was minimizing χ^2 function [20].

For each sample, all observed diffraction peaks were indexed to a ZnO wurtzite structure (space group *P63 mc*) and no other impurity phase was found, which indicates that Co ions successfully occupy the lattice site rather than interstitial ones. Average crystallite sizes were obtained by using Scherrer's equation [21] as follows:

$$d=\frac{0.9\lambda}{\beta\cos\theta}$$

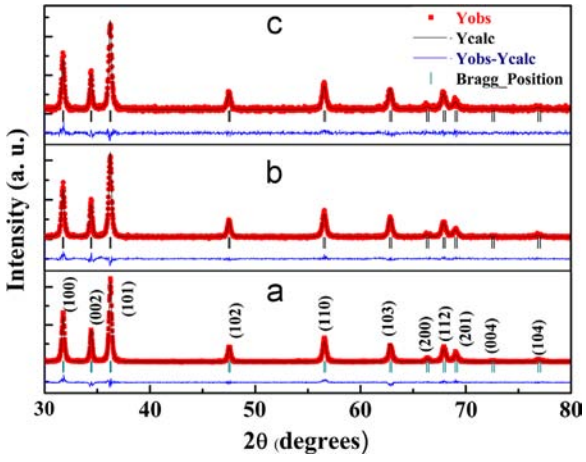

Fig. 1. Rietveld refined XRD patterns of $Zn_{1-x}Co_xO$ sintered at 400 °C: (a) $x=0.02$, (b) $x=0.04$ and (c) $x=0.06$.

where λ is the wavelength of X-rays, β is the half intensity width of the peak and θ is the diffraction angle. All high intensity peaks of the XRD pattern were used to calculate the average crystallite size. Crystal parameters and refinement factors calculated for hexagonal structure are summarized in Table 1. Lattice parameters as obtained for samples are in good agreement with literature [22]. The peak shift in the XRD pattern for Co doped ZnO is indiscernible which may be due to the quite similar ionic radius of Co^{2+} (0.58 Å) and Zn^{2+} (0.60 Å) ions in the tetrahedral coordination [23]. Thus, our results indicate the replacement of Zn ions by Co ions in ZnO matrix with 2+ valence state.

3.2. XPS results

To investigate the electronic and chemical state of the host and dopant elements, XPS measurements were undertaken. Samples were sputtered for 5 min at the base pressure of 10^{-6} Torr before performing XPS measurements. Fig. 3 shows the typical XPS survey spectra after Ar^{+} etching for 2% Co doped ZnO sintered at 400 °C and 500 °C. No extra peaks corresponding to any magnetic impurities other than Zn, Co and O atoms were detected. The analyzed XPS core level spectra of Zn 2p, Co 2p and O 1s are shown in Figs. 4–6, respectively in which overlapped bands were deconvoluted into separate peaks by Gaussian fitting using XPS peakfit software.

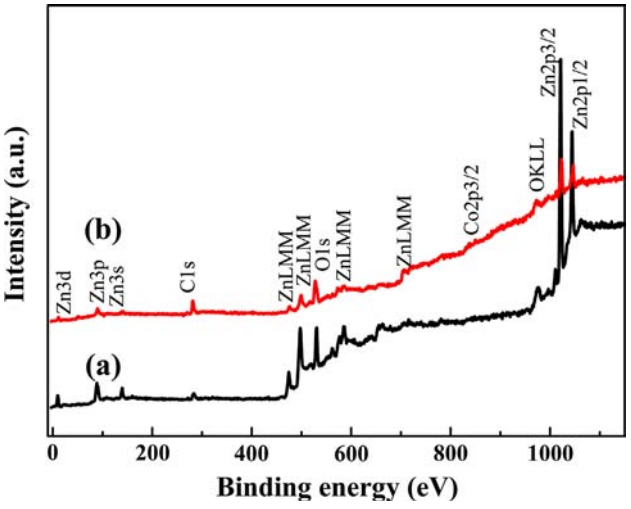

Fig. 3. XPS spectra after Ar^{+} etching for 2% Co doped ZnO sintered at (a) 400 °C and (b) 500 °C.

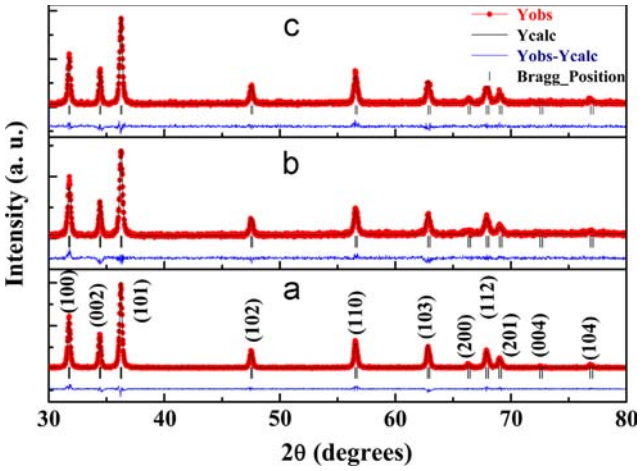

Fig. 2. Rietveld refined XRD patterns of $Zn_{1-x}Co_xO$ sintered at 500 °C: (a) $x=0.02$, (b) $x=0.04$ and (c) $x=0.06$.

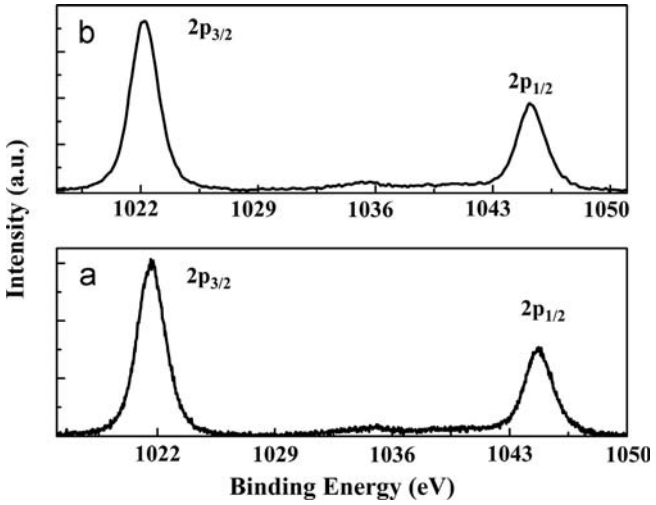

Fig. 4. XPS spectra of Zn $2p_{3/2}$ and $2p_{1/2}$ peaks for 2% Co doped ZnO along with the Gaussian fit sintered at (a) 400 °C and (b) 500 °C.

Table 1
The crystal parameters of Co doped ZnO samples from XRD.

Refined parameters	$Zn_{1-x}Co_xO$ sintered at 400 °C			$Zn_{1-x}Co_xO$ sintered at 500 °C		
	$x=0.02$	$x=0.04$	$x=0.06$	$x=0.02$	$x=0.04$	$x=0.06$
$a=b$ (Å)	3.254	3.251	3.253	3.251	3.250	3.252
c (Å)	5.206	5.206	5.207	5.207	5.204	5.206
V (Å)3	47.67	47.65	47.68	47.66	47.62	47.66
d (nm)	31.28	29.7	29.2	40.4	35.4	30.45
χ^2	1.23	1.12	1.10	1.19	1.14	1.16

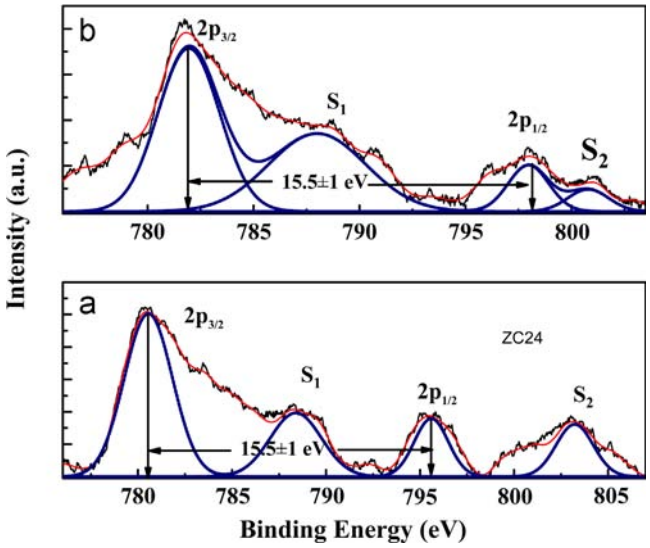

Fig. 5. XPS spectra of Co $2p_{3/2}$ and $2p_{1/2}$ peaks for 2% Co doped ZnO along with the Gaussian fit sintered at (a) 400 °C and (b) 500 °C.

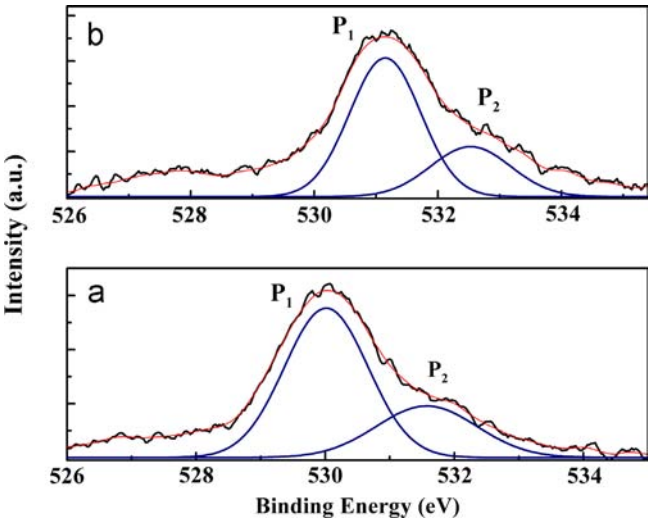

Fig. 6. The O 1s XPS spectra for the 2% Co doped ZnO along with Gaussian fits sintered at (a) 400 °C and (b) 500 °C.

The Zn 2p core level spectra for 2% Co doped ZnO sample sintered at 400 °C (Fig. 4) show two strong peaks at ~1021.7 eV and ~1044.8 eV corresponding to Zn $2p_{3/2}$ and Zn $2p_{1/2}$ states respectively. These peak positions are closely matching with the standard value for ZnO [24] indicating that Zn atoms are in a 2+ oxidation state. Energy values of Zn $2p_{3/2}$ peaks are below those of the metallic Zn. Thus the formation of Zn clusters is ruled out. But, it is interesting to note that both the peaks are shifted toward the higher binding energy for samples sintered at 500 °C. The binding energy position of both peaks shows a shift of around 1 eV, indicating a decrease in the valence electron density of Zn ions.

Fig. 5 shows the high resolution Co 2p XPS spectra of $Zn_{0.98}Co_{0.02}O$ sintered at different temperatures. All these samples show four major peaks, the Co $2p_{3/2}$ at ~780.43 eV, the Co $2p_{1/2}$ peak at ~795.9 eV and the corresponding satellite structures (S_1, S_2) at ~788.47 and 803.26 eV, respectively for the sample sintered at 400 °C. There is a shift (~1.3 eV) for both peaks sintered at 500 °C. This shift of Co peaks suggests that Co is indeed incorporated in the ZnO lattice. The peak corresponding to $2p_{3/2}$ located at ~780.43 eV is due to the Co^{2+} oxidation state [25].

The binding energy separation between Co $2p_{3/2}$ and Co $2p_{1/2}$ levels is determined to be 15.5 (±0.5) eV which is consistent with the divalent state of cobalt homogeneously surrounded by the oxygen tetrahedral [26]. If Co existed largely in the form of metal cluster in these samples, the energy difference of these peaks would have been 15.05 eV [27]. Thus the above findings demonstrate that Co atoms have successfully incorporated in tetrahedral sites of the wurtzite host matrix as substitutional impurities without forming any detectable impurity phase or Co clusters [28].

Fig. 6 shows the O 1s spectra of $Zn_{0.98}O_{0.02}O$ fitted with Gaussian. The O 1s can be separated into two peaks: the lower energy peak (labeled as P1) located at 530.03 eV [29] corresponds to O–Zn bonds, while the higher energy peak (labeled as P2) located at 531.57 eV can be attributed to O–H bonds due to exposure to air.

In the present study, we focus on the lower energy peak P1 rather than the higher energy peak P_2, because O–Zn band (peak P_1) is the most important in Co-doped ZnO. For our synthesized materials, the position of the peak P1 shifts to a higher binding energy (~1 eV) at higher sintering temperature as shown in Fig. 3b. In the case of the occupation of Co ions at Zn sites, it is reasonable to think that substitution of Co has an effect on the surrounding O–Zn binding energies through the effect of electron charges [30].

3.3. Optical and photoluminescence studies

The change in absorption peak due to doping indicates a change in the band structure. It is observed that absorption edges of $Zn_{1-x}Co_xO$ are at 375, 368 and 367 nm for $x=0.02$, 0.04 and 0.06 respectively when the samples were sintered at 400 °C and at 379, 375 and 372 for the samples sintered at 500 °C (Fig. 7). The position of the absorption spectra is observed to shift toward lower wavelength side with increase in Co concentration, which is indicating an increase in band gap with Co doping. This blueshift behavior can in principle be explained by the Moss–Burstein band filling effect, which is frequently observed in n-type semiconductors [31].

The PL spectroscopy is an effective method to investigate the presence of defects in semiconductors. PL spectra of Co doped ZnO samples were taken at room temperature with the excitation wavelength of 325 nm which are shown in Fig. 8a and b fitted with the Gaussian.

PL spectra show emission band in the UV and visible region with asymmetric line shape. Experimental data are fitted with asymmetric three constituent peaks (A–C) summarized in Table 2. PL spectra of $Zn_{1-x}Co_xO$ samples

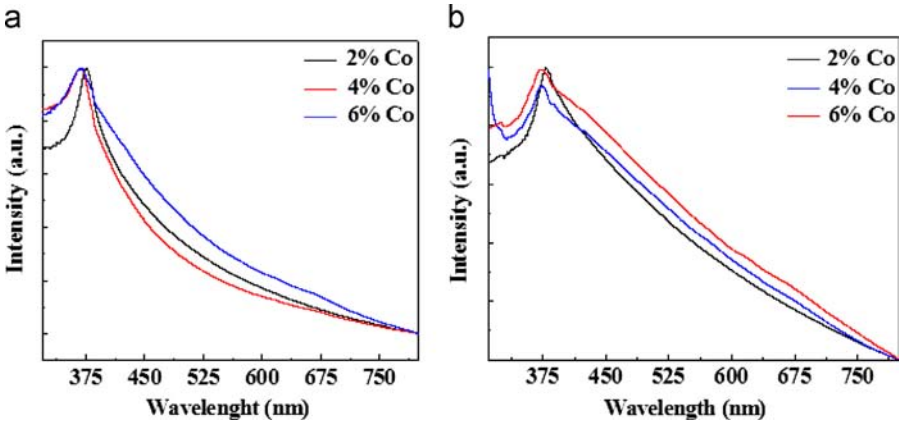

Fig. 7. Absorption spectra of $Zn_{1-x}Co_xO$ samples sintered at (a) 400 °C and (b) 500 °C.

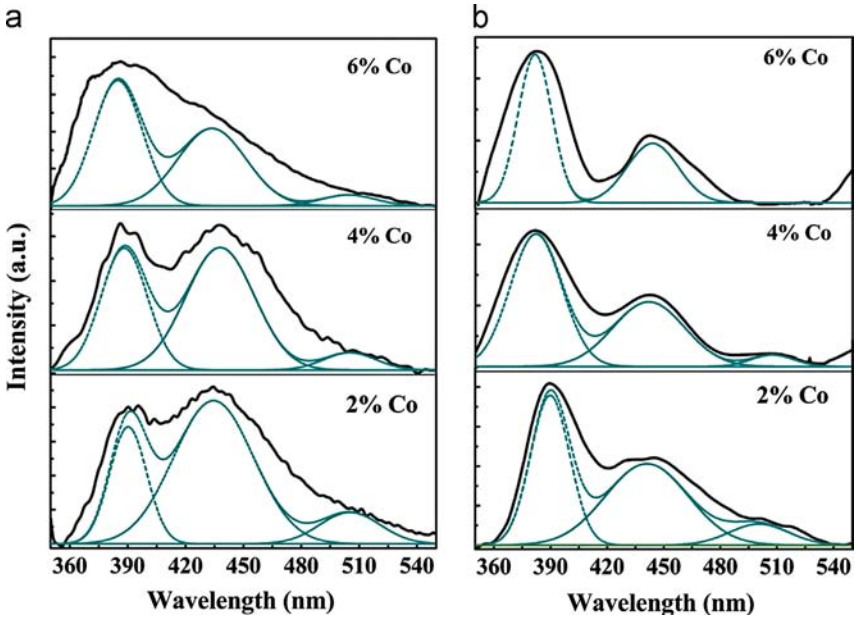

Fig. 8. PL spectra of Co doped ZnO samples sintered at (a) 400 °C and (b) 500 °C with the Gaussian fit.

Table 2
Peak position of the samples from PL spectra.

Peak positions	$Zn_{1-x}Co_xO$ sintered at 400 °C			$Zn_{1-x}Co_xO$ sintered at 500 °C			Peak identity
	$x=0.02$	$x=0.04$	$x=0.06$	$x=0.02$	$x=0.04$	$x=0.06$	
A	390	386	384	389	381	378	NBE
B	434	438	438	442	441	439	Zn_i
C	508	520	510	503	509	–	V_0

consist of a strong excitonic recombination UV emission peak centered at ~390 nm corresponding to the near band emission [32]. Apart from this, a strong blue emission peak centered at ~434 and a broad D band emission, centered at ~508 nm are observed [33]. The PL spectra show a slight shift in peak positions with increase in the cobalt concentration as well as in the sintering temperature. The UV emission related to the near band edge [NBE] emission slightly shifts toward the lower wavelength with Co doping as shown in Table 2, i.e. the UV emission peak is found to blue shift with the increase in cobalt concentration.

The observed strong visible emission is believed to be originated from the deep level of Co doped ZnO and is due to the presence of singly ionized oxygen vacancies (V_0) and

Zn interstitials (Zn_i) [33–35]. If we are concerned about the sintering temperature, D band emission which corresponds to the oxygen vacancy is completely suppressed for the sample $Zn_{0.94}Co_{0.06}O$ sintered at 500 °C.

3.4. Magnetization

Room temperature DC magnetic field dependent magnetization curves (M versus H) for samples sintered at 400 °C and 500 °C are shown in Fig. 9. RTFM is observed in all samples.

Decrease in the remanent magnetization and the coercive field for 6% Co doped ZnO sintered at 500 °C is observed. Also, the value of magnetization decreased at higher sintering temperature.

The origin of ferromagnetism in oxide based DMS materials is still not clear as there is an incomplete understanding whether it is an extrinsic effect due to direct interaction between the local moments in magnetic impurity clusters or is indeed an intrinsic property caused by exchange coupling between the spin of the carriers and local magnetic moments. There are various theories proposed in literature to explain the mechanism of the origin of RTFM in DMSs [36–39].

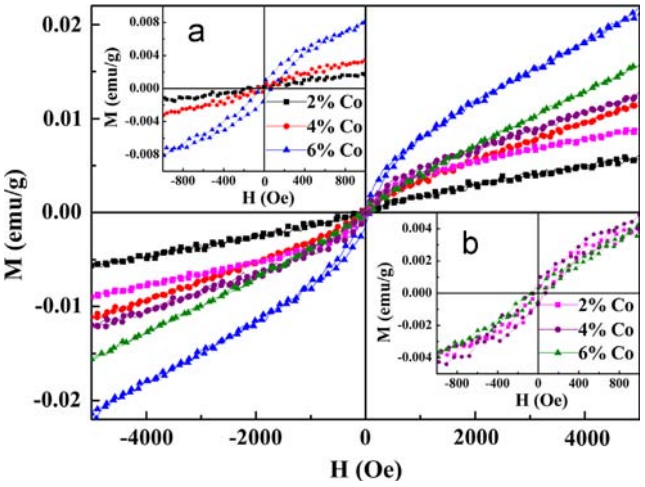

Fig. 9. M–H curves of Co doped ZnO samples inset shows samples sintered at (a) 400 °C and (b) 500 °C.

As oxygen vacancies are inherently present in our samples due to the stabilization of the structure, it can be predicted that oxygen vacancy defect constituted bound magnetic polarons (BMPs) which are one of the promising candidates for the origin of RTFM in this system. Within the BMP model, the large density of oxygen vacancy and more doping help to produce more BMPs, which yield a greater overall volume occupied by BMPs, leading to the overlap of BMPs and enhancing ferromagnetism. The evolution observed in our case is increase in magnetization with increase in oxygen vacancies, indicating that percolation of BMPs may be responsible for ferromagnetism [33].

In order to further understand the origin of magnetic properties, suitability of the BMP model is checked by fitting the M–H data to the following equation [39]:

$$M = M_0 L(x) + \chi_m H$$

where the first term is to account for the BMP contribution and the second term is due to the observed paramagnetic contribution at higher field. According to the above equation, the samples are predicted as a mixture of BMPs where localized charge carriers strongly interact with the doped transition element over the Bohr radius and the paramagnetic matrix [40]. Here, the spontaneous moment of the system is given by $M_0 = Nm_s$, N is the number of BMPs involved and m_s is the spontaneous magnetic moment per BMP. $L(x) = \coth(x) - (1/x)$ is the Langevins function with $x = m_{eff}H/(k_BT)$, where m_{eff} is the true spontaneous moment per BMP. At high temperature, the interaction between the BMPs can be ignored and $m_s = m_{eff}$ can be taken. χ_m is the susceptibility of the matrix. The

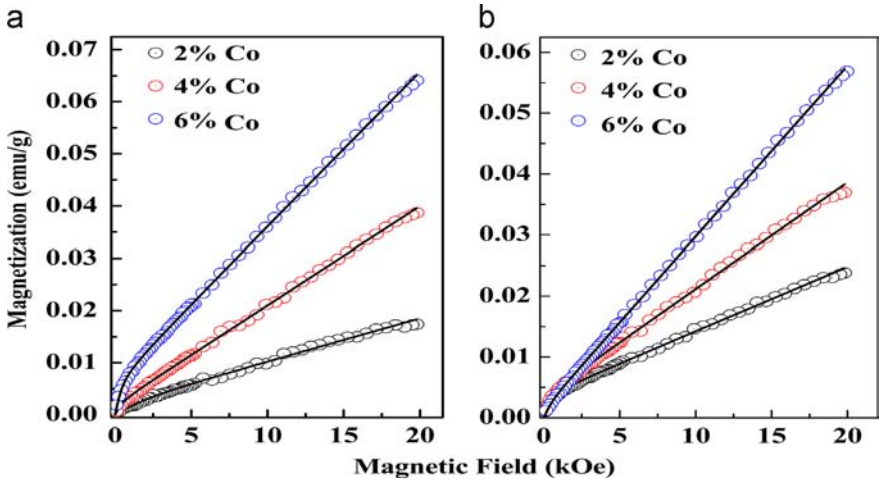

Fig. 10. Initial portion of the M–H curve fitted with the BMP model for samples sintered at (a) 400 °C and (b) 500 °C. Symbols are for experimental data and the solid line is a fit with the BMP model.

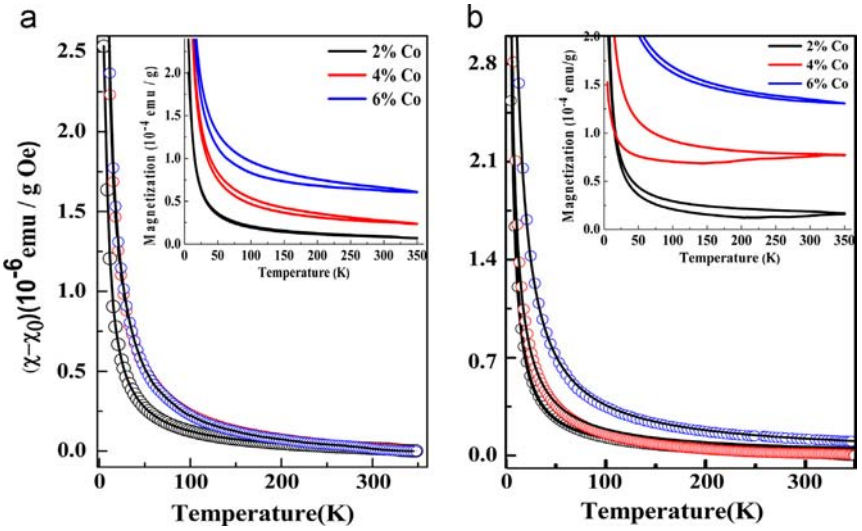

Fig. 11. Temperature variation of magnetic susceptibility χ for 2%, 4% and 6% Co doped ZnO samples sintered at (a) 400 °C and (b) 500 °C. The solid line is fit Curie–Weiss law. The inset shows the MT curve for field cooled (FC) and zero field cooled (ZFC) cases at $H=100$ Oe in which distinct bifurcation of FC and ZFC curves can be seen well above at room temperature.

parameters M_0, m_{eff} and χ_m are variables during the fit. The experimental data along with the fitted data are shown in Fig. 10a and b in which fitted data closely follow the experimental data and fitted parameters are tabulated in Table 3. The spontaneous moment per BMP is found to the order of 10^{-17} emu. The number of BMPs which were determined from M_0 and m_{eff} values are found to be of the order of 10^{16}/cm^3 which is very small to the concentration necessary for prelocation in ZnO. The required concentration of BMPs is in the range of 10^{20}/cm^3 which is four orders larger than the observed value [33]. Thus the BMP model alone is insufficient to explain RTFM in the Co doped ZnO system.

For further investigation of magnetic ordering in Co doped ZnO system, we tried to explore it with the help of modified Curie–Weiss law [21]. Fig. 11a and b shows the susceptibilities under a magnetic field of 100 Oe for $Zn_{(1-x)}Co_xO$ samples ($x=0.02$, 0.04 and 0.06) sintered at 400 °C and 500 °C respectively where the solid lines are the fit to the modified Curies–Weiss law:

$$\chi = \chi_0 + \frac{C_M}{T-\theta}$$

where χ_0 represents the non-paramagnetic contributions, χ is the susceptibility of the material, $C_M(=C_0x)$ is the Curie–Weiss temperature and $\theta(=\theta_0x)$ is the Curie constant per gram. x is the transition metal concentration. Constants C_0 and θ are defined as

$$C_0 = \frac{Ng_{eff}^2\mu_B^2 S(S+1)}{3k_B}$$

$$\theta = \frac{2zS(S+1)J_1}{3k_B}$$

where N is the number of cations per gram, g_{eff} is the effective gyromagnetic factor of Co ions, $S=3/2$ is the spin for Co^{2+}, μ_B is the Bohr magneton, z is the number of nearest neighbors ($z=12$ in the wurtzite structure), J_1 is the effective exchange integral constant and k_B is the Boltzmann constant. The values of θ and C are obtained by fitting the data using the Curie–Weiss law which are tabulated in Table 3. Curie–Weiss temperature θ is obtained to be negative for all samples but values are very small indicating the existence of weak antiferromagnetic (AFM) exchange interaction between Co^{2+} ions, and the AFM coupling increased with increasing cobalt content [41,42].

Weak ferromagnetic behavior is observed for all samples as shown in M–H curve, implying that a small fraction of Co ions gives rise to observed ferromagnetism. Therefore, it is reasonable to conclude that three forms of Co ions exist in $Zn_{1-x}Co_xO$ samples: (i) AFM coupled Co ions with at least one neighboring Co ion, (ii) isolated Co ions, which behave paramagnetically and contribute to magnetization at low temperature and (iii) the Co ions within BMPs which couple ferromagnetically via the donor electron associated with defects and also make a partial contribution to the magnetization [43,44].

4. Conclusions

In summary, polycrystalline $Zn_{1-x}Co_xO$ ($x=0.02$, 0.04 and 0.06) samples have been synthesized by the simple sol–gel method. XRD measurements reveal that all the samples have hexagonal wurtzite structure and no secondary phases were detected. XPS results reveal that Co atoms have successfully incorporated in tetrahedral sites of the wurtzite host matrix without forming any detectable impurity phase. Blue shift in the band gap has been observed which may be due to the Moss–Burstein band filling effect. Magnetic measurements show a weak

Table 3
List of parameters obtained from experimental M–H curve along with the fitted data in the BMP model and Curie–Weiss fitting.

Samples $Zn_{1-x}Co_xO$	Experimental data			Fitting parameters extracted from the BMP model				Fitting parameters extracted from Curie–Weiss law	
	$M_r \times 10^{-4}$ (emu/g)	H_c (Oe)	S	$M_0 \times 10^{-3}$ (emu/g)	$m_{eff} \times 10^{-17}$ (emu)	$\chi_m \times 10^{-7}$ (eg s)	$N \times 10^{16}$ (cm^3)	θ (K)	$C \times 10^{-5}$ (emu K/g)
Samples sintered at 400 °C									
$x=0.02$	3.25	149.9	3/2	2.2	4.3	8.2	0.0287	−0.38	1.9
$x=0.04$	4.56	76.9	3/2	2.0	0.21	1.89	0.534	−0.58	2.6
$x=0.06$	7.17	40.3	3/2	6.0	0.19	2.96	0.177	−1.25	2.7
Samples sintered at 500 °C									
$x=0.02$	4.53	50.6	3/2	3.7	0.22	1.05	0.943	−0.52	1.3
$x=0.04$	6.99	70.6	3/2	3.8	0.21	1.74	1.02	−0.68	1.9
$x=0.06$	4	43.4	3/2	1.7	0.19	2.8	0.502	−1.08	3.6

ferromagnetic behavior at room temperature with some antiferromagnetic coupling.

Acknowledgments

One of the authors, RK, is thankful to Dr. Govind Gupta (National Physical Laboratory, New Delhi, India) for valuable suggestions and support.

References

[1] H. Ohno, Science 281 (1998) 951.
[2] T. Dietl, H. Ohno, F. Matsukura, J. Cibert, D. Ferrand, Science 287 (2000) 1019.
[3] Y. Matsumoto, M. Murakami, T. Shono, T. Hasegawa, T. Fukumura, M. Kawasaki, P. Ahmet, T. Chikyow, S. Koshihara, H. Koinuma, Science 291 (2001) 854.
[4] H. Yan, J. Johnson, M. Law, R. He, K. Knutsen, J.R. Mckinney, J. Pham, R. Saykally, P. Yang, Advanced Materials 15 (2003) 1907.
[5] S.J. Pearton, D.P. Norton, K. Ip, Y.W. Heo, T. Steiner, Progress in Materials Science 50 (2005) 293.
[6] T. Dietl, Journal of Applied Physics 89 (2001) 7437.
[7] K. Ueda, H. Tabata, T. Kawai, Applied Physics Letters 79 (2001) 988.
[8] H. Saeki, H. Tabata, T. Kawai, Solid State Communications 120 (2001) 439.
[9] S.E. Park, H.-J. Lee, C.R. Cho, Y.C. Cho, S. Cho, S.-Y. Jeong, Applied Physics Letters 80 (2002) 4187.
[10] Y.M. Cho, W.K. Choo, H. Kim, D. Kim, Y.E. Ihm, Applied Physics Letters 80 (2002) 3358.
[11] Z. Jin, T. Fukumura, M. Kawasaki, K. Ando, H. Saito, T. Sekiguchi, Y.Z. Yoo, M. Murakami, Y. Matsumoto, T. Hasegawa, H. Koinuma, Applied Physics Letters 78 (2001) 3824.
[12] T. Zhu, W.S. Zhan, Applied Physics Letters 89 (2006) 022508.
[13] S. Koleski, B. Dabrowski, J. Mais, Journal of Applied Physics 95 (2004) 5.
[14] K. Sato, H. Katayama-Yoshida, Japanese Journal of Applied Physics 40 (2) (2001) L334.
[15] C. Liu, F. Yun, H. Morkoc, Journal of Materials Science: Materials in Electronics 16 (2005) 555.
[16] F. Pan, C. Song, X.J. Liu, Y.C. Yang, F. Zeng, Materials Science and Engineering Reports 62 (2008) 1.
[17] J.M.D. Coey, M. Venkatesan, C.B. Fitzgerald, Nature Materials 4 (2005) 173.
[18] D.C. Kundaliya, S.B. Ogale, S.E. Lofland, S. Dhar, C.J. Metting, S.R. Shinde, Z. Ma, B. Varughese, K.V. Ramanujachary, L. Salamanca Riba, T. Venkatesan, Nature Materials 3 (2004) 709.
[19] T. Dietl, T. Andrearczyk, A. Lipinska, M. Kiecana, M. Tay, Y. Wu, Physical Review B 76 (2007) 155312.
[20] S. Thota, T. Dutta, J. Kumar, Journal of Physics: Condensed Matter 18 (2006) 2473.
[21] S. Ghoshal, P.S. Anil Kumar, Journal of Magnetism and Magnetic Materials 320 (2008) L93.
[22] H.B. Carvalho, M.P.F. de Godoy, R.W.D. Paes, M. Mir, A. Ortiz de Zevallos, F. likawa, M.J.S.P. Brasil, V.A. Chitta, W.B. Ferraz, M.A. Boeselli, A.C.S. Saibioni, Journal of Applied Physics 108 (2010) 033914.
[23] X. Wang, R. Zheng, Z. Liu, J. Xu, S.P. Ringer, Nanotechnology 19 (2008) 455702.
[24] R.K. Singhal, M. Dhawan, S.K. Gaur, S.N. Dolia, S. Kumar, T. Shripathi, U.P. Deshpande, Y. Xing, E. Saitovitch, K.B. Garg, Journal of Alloys and Compounds 477 (2009) 379.
[25] R.K. Singhal, A. Samariya, Y.T. Xing, S. Kumar, S.N. Dolia, T. Shripathi, U.P. Deshpande, E. Saitovitch, Journal of Alloys and Compounds 496 (2010) 324.
[26] X. Huang, G. Li, L. Duan, L. Li, X. Dou, L. Zhang, Scripta Materialia 60 (2009) 984.
[27] C.D. Wanger, W.M. Riggs, L.E. Davis, J.F. Moulder, in: G.E. Mulenberg (Ed.), Hand Book of X-ray Photoelectron Spectroscopy, Physical Electronics Division, Minnesota, USA, 1979, p. 78.
[28] M. Naeem, S.K. Hasanain, M. Kobayashi, Y. Ishida, A. Fujimori, S. Buzby, S. Ismat Shah, Nanotechnology 17 (2006) 2675.
[29] J.F. Moulder, W.F. Stickle, P.E. Sobol, K.D. Bomben, in: Handbook of X-ray Photoelectron Spectroscopy, Physical Electronics, Inc., USA, 1995 (Chapters 8, 27 and 30).
[30] Y.Z. Peng, T. Liew, W.D. Song, C.W. An, K.L. Teo, T.C. Chong, Journal of Superconductivity: Incorporating Novel Magnetism 18 (2005) 1.
[31] E. Burstein, Physical Review 93 (1954) 632.
[32] Y.C. Kong, D.P. Yu, B. Zhang, W. Fang, S.Q. Feng, Applied Physics Letters 78 (2001) 407.
[33] B. Pal, P.K. Giri, Journal of Applied Physics 108 (2010) 084322.
[34] R. Elilarassi, G. Chandrasekaran, Journal of Materials Science: Materials in Electronics 22 (2011) 751.
[35] C. Li, G. Fang, Q. Fu, F. Su, G. Li, X. Wu, X. Zhao, Journal of Crystal Growth 292 (2006) 19.
[36] Y. Sun, N.G. Ndifor-Angwafor, D.J. Riley, M.N.R. Ashfold Chemical Physics Letters 431 (2006) 352.
[37] H.T. Ng, B. Chen, J. Li, J. Han, M. Meyyappan, J. Wu, S.X. Li, E.E. Haller, Applied Physics Letters 82 (2003) 2023.

[38] A. Van dijken, E.A. Meulenkamp, D. Vanmaekelbergh, A. Meijerink, Journal of Luminescence 87–89 (2000) 454.
[39] C. Chiorescu, J.L. Cochin, J.J. Neumeier, Physical Review B 76 (2007) 0202404®.
[40] T. Bora, B. Samantaray, S. Mohanty, S. Ravi, IEEE Transactions on Magnetics 47 (2011) 3991.
[41] J. Spalck, A. Lewicki, Z. Tarnawski, J.K. Furdyna, R.R. Galazka, Z. Obuszko, Physical Review B 33 (1986) 3407.
[42] S. Kolesnik, B. Dabrowski, J. Mais, Journal of applied physics 95 (2004) 2582.
[43] Z.M. Tian, S.L. Yuan, S.Y. Yin, S.Q. Zhang, H.Y. Xie, J.H. Miao, Y.Q. Wang, J.H. He, J.Q. Li, Journal of Magnetism and Magnetic Materials 320 (2008) L5.
[44] K.M. Reddy, J. Hays, S. Kundu, L.K. Dua, P.K. Biawas, C. Wang, V. Shutthanandan, M.H. Engelhard, X. Mathew, A. Punnoose, Journal of Materials Science: Materials in Electronics 18 (2007) 1197.